

Large-Scale Fabrication of Robust Artificial Skins from a Biodegradable Sealant-Loaded Nanofiber Scaffold to Skin Tissue via Microfluidic Blow-Spinning

Tingting Cui, Jiafei Yu, Qing Li, Cai-Feng Wang, Su Chen,* Weijie Li, and Gefei Wang*

Given that many people suffer from large-area skin damage, skin regeneration is a matter of high concern. Here, an available method is developed for the formation of large-area robust skins through three stages: fabrication of a biodegradable sealant-loaded nanofiber scaffold (SNS), skin tissue reconstruction, and skin regeneration. First, a microfluidic blow-spinning strategy is proposed to fabricate a large-scale nanofiber scaffold with an area of 140 cm × 40 cm, composed of fibrinogen-loaded polycaprolactone/silk fibroin (PCL/SF) ultrafine core–shell nanofibers with mean diameter of 65 nm. Then, the SNS forms, where the gelling reaction of fibrin sealant occurs *in situ* between thrombin and fibrinogen on PCL/SF nanofiber surface, to promote the migration and proliferation of fibroblasts, accelerating skin regeneration. Through an *in vivo* study, it is shown that the SNS can rapidly repair acute tissue damage such as vascular bleeding and hepatic hemorrhage, and also promote angiogenesis, large-area abdominal wall defect repair, and wound tissue regeneration for medical problems in the world. Besides, it avoids the risk of immune rejection and secondary surgery in clinical applications. This strategy offers a facile route to regenerate large-scale robust skin, which shows great potential in abdominal wall defect repair.

The human skin provides a vast physical barrier to protect our internal tissues from mechanical damage, microbial infection, ultraviolet radiation and extreme temperature. The skin, as the external epithelium of the body, sustains organismal homeostasis, and repairs injuries throughout a life.^[1] Mimicking skins to develop promising artificial materials with advanced skin potential is highly desirable. To this end, a number of foam-like structural materials (porous foams^[2]), film-like structural

materials (biocompatible membranes,^[3] nanofiber scaffold^[4,5]), hydrogel-like structural materials (self-healing hydrogel,^[6] injectable hydrogel^[7]), and hydrocolloid-like structural materials (carboxymethyl cellulose,^[8] alginate^[9]) have been developed. Among them, nanofiber scaffolds play a significant role in skin regeneration, because they can behave as extracellular skin-like matrices for better cell recruitment and easy incorporation of bioactive molecules, enhancing the permeation of nutrients and oxygen.^[10] However, in most cases, the skin scaffolds are mainly used for small-area wound, along with inferior flexibility, poor biocompatibility, and cell adhesion. Therefore, they would never be comparable to human skins unless new skin regeneration materials are developed—particularly those associated with preferable biocompatibility, tissue regeneration, and non-surgical interventions.^[11]

So far, much efforts have been devoted to the preparation of nanofiber scaffolds

for skin regeneration. The fabrication approach of nanofiber scaffolds is best illustrated by electrospinning method.^[12] The as-employed materials including polycaprolactone (PCL),^[13] poly(lactic acid),^[14] poly (L-lactide),^[15] silk fibroin (SF),^[16] poly(lactic-co-glycolic acid) (PLGA),^[17] chitosan,^[18] and collagen,^[19] have been applied in various wound healing applications, skin regeneration,^[20–22] and viscera protects.^[23] Among these biopolymers, PCL is known for its biocompatibility, and favorable mechanical properties. However, PCL is not sufficiently hydrophilic, making it lack cell recognition signals, limiting its microenvironment required for cell adhesion, proliferation, and biomaterial–cell interactions.^[24] To ameliorate the disadvantages, we introduce SF and fibrinogen since they are promising biomaterials amongst natural polymers for tissue scaffold and tissue regeneration, and they play an important role in enhanced cell adhesion, migration, proliferation and differentiation in cell culturing which have been verified.^[25] In this respect, Wang et al. reported a SF-Mel/PCL nanofiber film via electrospinning for promoting wound healing.^[26] Ru et al. proposed a PLGA/SF composite nanofiber scaffold for skin regeneration.^[27] Among them, most of the scaffolds were usually fabricated via electrospinning,^[28–30] solution blowing spinning (SBS),^[31] and microfluidic spinning,^[32] while only several examples were realized by microfluidic

T. T. Cui, Dr. Q. Li, Dr. C.-F. Wang, Prof. S. Chen
State Key Laboratory of Materials-Oriented Chemical Engineering
College of Chemical Engineering
Jiangsu Key Laboratory of Fine Chemicals and Functional Polymer Materials

Nanjing Tech University
Nanjing 210009, P. R. China
E-mail: chensu@njtech.edu.cn

J. F. Yu, W. J. Li, Prof. G. F. Wang
Department of General Surgery
Jinling Hospital
Nanjing Medical University
Nanjing 210002, P. R. China
E-mail: Gefei_W@163.com

 The ORCID identification number(s) for the author(s) of this article can be found under <https://doi.org/10.1002/adma.202000982>.

DOI: 10.1002/adma.202000982

blow-spinning (MBS).^[33] In addition, it seems to be far from easy to implement the preparation of nanofiber scaffolds at large-area using the current fiber spinning techniques, such as electrospinning,^[28–30] and microfluidic spinning.^[34] Among these methods, the SBS and MBS methods are the most likely to realize the industrialization of nanofibers. Moreover, the nanofibers produced by MBS can precisely control the fiber diameter and orientation through mechanical relocation and the design of special microfluidic chip,^[35] whereas the research of SBS mainly focuses on the relationship between specific process parameters (gas pressure, flow rate), solution parameters (solvent, polymer solution concentration, molecular weight), and fiber diameter.^[36] Therefore, if performed in a reliable scale-up manner and precisely control the fiber diameter, such fiber spinning strategies would benefit in this field, especially in large-area skin regeneration.

Recently, various clinically surgical sealants, such as fibrin,^[37] glutaraldehyde,^[38] cyanoacrylate,^[39] and poly(ethylene glycol) hydrogel-based materials,^[40] draw much attention because

they could ensure a moist skin healing environment and skin tissue regeneration. For instance, Kofinas et al. developed a body temperature responsive surgical sealant via handheld SBS.^[41] However, synchronous coupling of the sealants to the nanofiber scaffold is still rarely reported. we propose that this synchronous coupling could combine the advantages of both a nanofiber scaffold with strong mechanical properties and a sealant maintaining a moist wound healing environment.

In this work, we demonstrate an available strategy for large-area skin regeneration derived from biodegradable fibrin-sealant-loaded nanofiber scaffold (SNS). The transition goes through three stages: fabrication of large-area biodegradable SNS; formation of skin tissue; and skin regeneration. Initially, the method focuses on fabrication of a large-area fibrinogen-loaded PCL/SF nanofiber scaffold (area of $40 \times 140 \text{ cm}^2$, mean diameter of 65 nm, finest diameter of 44 nm) via a new MBS for the first time (Figure 1a). Then, we create a large-area SNS which can promote skin regeneration via a series of biological events (hemostasis, inflammation, proliferation, and

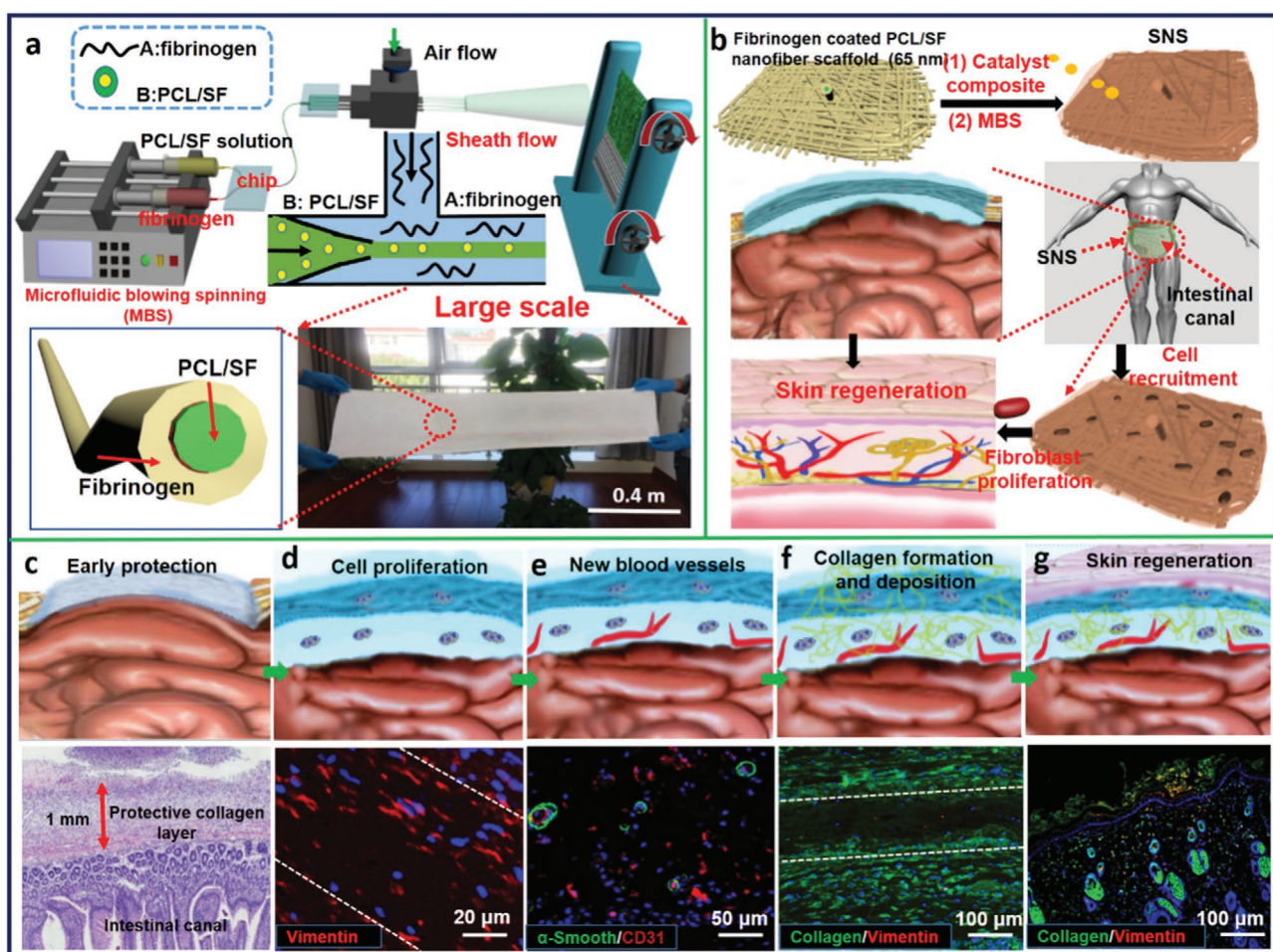


Figure 1. Schematic preparation of fibrinogen-coated PCL/SF nanofiber scaffold and fibrin-sealant-loaded nanofiber scaffold (SNS) promoting skin regeneration. a) Schematic illustration for the preparation of biodegradable fibrinogen-coated PCL/SF nanofiber scaffold, composed of fibrinogen-coated PCL/SF core–shell nanofibers by MBS. b) Three stages toward abdominal skin regeneration: fabrication of biodegradable SNS, skin tissue reconstruction, and skin formation. c–g) Schematic illustration (upper) and the corresponding experimental results (lower) for skin construction in abdominal wall defect: c) early protection mechanism via forming collagen layer; d) cell proliferation; e) regeneration of new blood vessels; f) collagen formation and deposition; and g) skin renewal. White wireframe area represents SNS area.

remodeling^[20]) for the first time. Here, an MBS method is used to assist the *in situ* gelation reaction of thrombin and fibrinogen by blowing a solution of catalyst composite (containing thrombin) on the as-prepared fibrinogen-coated PCL/SF nanofiber scaffold, resulting in the formation of fibrin sealant on the surface of PCL/SF nanofibers. Thus, the SNS has the synergistic advantage of nanofiber scaffold and fibrin sealant. Especially, the specific surface area of fibrin sealant is greatly improved, so the SNS are favorable for recruitment and proliferation of fibroblasts (Figure 1b–d). Besides, the high strength of fibrinogen-coated PCL/SF nanofiber scaffold and the tissue adhesion of fibrin sealant enable SNS to effectively cover the wound surface and replace the skin at the defect to resist the invasion of pathogens, and excellent cell recruitment and biodegradation features allow the formation of skin tissue into skin regeneration through the deposition of collagen and the formation of new blood vessels (Figure 1e–g). The large-scale fabrication of SNS through MBS offer important guiding significance and universal applicability for the construction of large-area skin regeneration materials. More importantly, we further verify that the as-prepared SNS can effectively promote large area abdominal skin repair through *in vivo* experiments, solve the easy infection problem as well as avoid the risk of immune rejection and secondary surgery. Also, it may be a promising candidate for solution of large-area wound repair medical problem, and thus more parallel works, for instance, large-area burns and battlefield skin damage, may follow.

The large-scale formation of skin regeneration starts from synthesis of nanofiber scaffolds. Initially, we fabricated a large area ($40 \times 140 \text{ cm}^2$) nanofiber scaffold composed of core–shell nanofibers with PCL/SF as the core and fibrinogen as the shell segment via MBS (Figures S1 and S2 and Movie S1, Supporting Information). The fiber diameters of the nanofiber scaffolds (PCL:Sf = 5:5 w/w) range from 44 to 96 nm (Figure 2a), which might be the finest spinning polymer fibers currently reported.^[28] It should be noted that the diameters and morphologies can be easily adjusted by varying the PCL/SF weight ratios and spinning parameters (PCL/SF weight ratios, acceptance distance, air pressure) (Figures S3–S6, Supporting Information). We then run several experiments to compare MBS with electrospinning and microfluidic spinning methods. It is noticed that the average diameter of fibers obtained from electrospinning method is around 230 nm (Figure 2b), while it is 1.3 μm from microfluidic spinning method (Figure 2c). Based on these results, we summarized the minimum fiber diameters from four spinning methods, including electrospinning, SBS,^[42] microfluidic spinning and our MBS method, which are 164 nm, 150 nm, 0.8 μm and 44 nm, respectively (Figure 2d). We then cultured fibroblasts stained with F-actin on nanofiber scaffolds with different fiber diameters prepared by the MBS (Figure S7, Supporting Information) and nanofiber scaffolds prepared by different spinning methods (Figure S8, Supporting Information). Importantly, F-actin was essential for cell movement and contraction, which were arranged in parallel directions with a long linear arrangement along the main cell axis of the whole cytoplasm. The results reveal that the finest nanofibers spun via MBS could increase the migration of fibroblasts, effectively facilitate the fibroblast attachment, proliferation and growth due to the large specific surface area. In

addition, the MBS-induced nanofiber scaffold displays porous structure (the magnified SEM image in Figure 2a; Figure S9, Supporting Information), suggesting a certain permeability of the nanofiber scaffold. We investigated the temporal evolution of water contact angle of the fibrinogen-coated nanofiber scaffold (Figure 2e). As a water drop was placed on the fibrinogen-coated nanofiber scaffold, a water contact angle of 76° was observed at 0 s, while it sharply declined to 2° within 32 s. These features indicate good hydrophilicity and permeability of the nanofiber scaffold. The nanofiber scaffold is flexible enough to be folded into a butterfly shape (Figure S10, Supporting Information), providing great potential in practical applications.

Subsequently, we sprayed the catalyst composite (containing thrombin) onto the fibrinogen-coated SF/PCL nanofiber scaffolds to generate SNS by *in situ* reaction within 2 minutes^[43] (Figure 2f). The SEM image proves that the fibrinogen of shell structure was gelatinized *in situ* with thrombin and form fibrin sealant. Moreover, the colloidal fusion made the nanofibers gather to form clusters (Figure 2g,h). In addition, the fluorescence staining experiment revealed that a large number of fibroblasts (marker is a vimentin that has been dyed red) were recruited on the SNS scaffold (Figure 2h, right). It should be noted that the mechanical strength of SNS (Stress: 8.45 MPa, Young modulus: 1.93 MPa) is enhanced after the reaction (Table S1 and Figure S11, Supporting Information), which is comparable to the commercial product (PP mesh, Stress: 8.05 MPa, Young modulus: 3.94 MPa) and slightly inferior to real mouse skin (Stress: 11.05 MPa, Young modulus: 2.6 MPa) (Figure S12, Supporting Information). Furthermore, we tested the pore size of fibrinogen-coated PCL/SF nanofiber scaffolds before and after the addition of catalyst composite using an aperture distributor. It was found that the average pore diameter of the fibrinogen-coated PCL/SF nanofiber scaffolds decreased from 3.42 to 2.50 μm after the addition of catalyst composite (Figure S9, Supporting Information). In addition, we further analyzed the morphology and air permeability of the SNS before and after the formation of the SNS by SEM and gas permeability measurements^[44] (Figure S13, Supporting Information). Nitrogen permeability of the SNS ($164.635 \text{ m}^3/\text{m}^2 \text{ h kPa}$) formed by the *in situ* reaction is much larger than that of the PCL/SF nanofiber scaffold directly bounded with fibrin sealant (FS@PCL/SF nanofiber scaffold, $50.999 \text{ m}^3/\text{m}^2 \text{ h kPa}$). Figure S14, Supporting Information, shows water absorption ration of SNS at different pH values of 5 and 8, respectively. The SNS has good water absorption ability, and its water absorption ration approaches a constant after 14 hours of swelling. This feature suggests that the SNS is capable of absorbing wound exudate. Moreover, the SNS exhibits good degradability. A total weight decrease of $\approx 78\%$ for 7 days under a temperature of 80 °C and a humidity of 55% was observed (Figure S15, Supporting Information); the linear degradation profile is consistent with surface erosion in contrast to bulk erosion. The *in vivo* degradation test was also performed, suggesting that at least seven months are needed for SNS to degrade *in vivo* (Figure S16, Supporting Information). Importantly, we also investigated the SNS formation mechanism via the reaction between the catalyst composite (containing thrombin) and the fibrinogen on the surface of PCL/SF nanofibers. The nanofiber scaffold contains fibrinogen components, and fibrinogen can react with thrombin

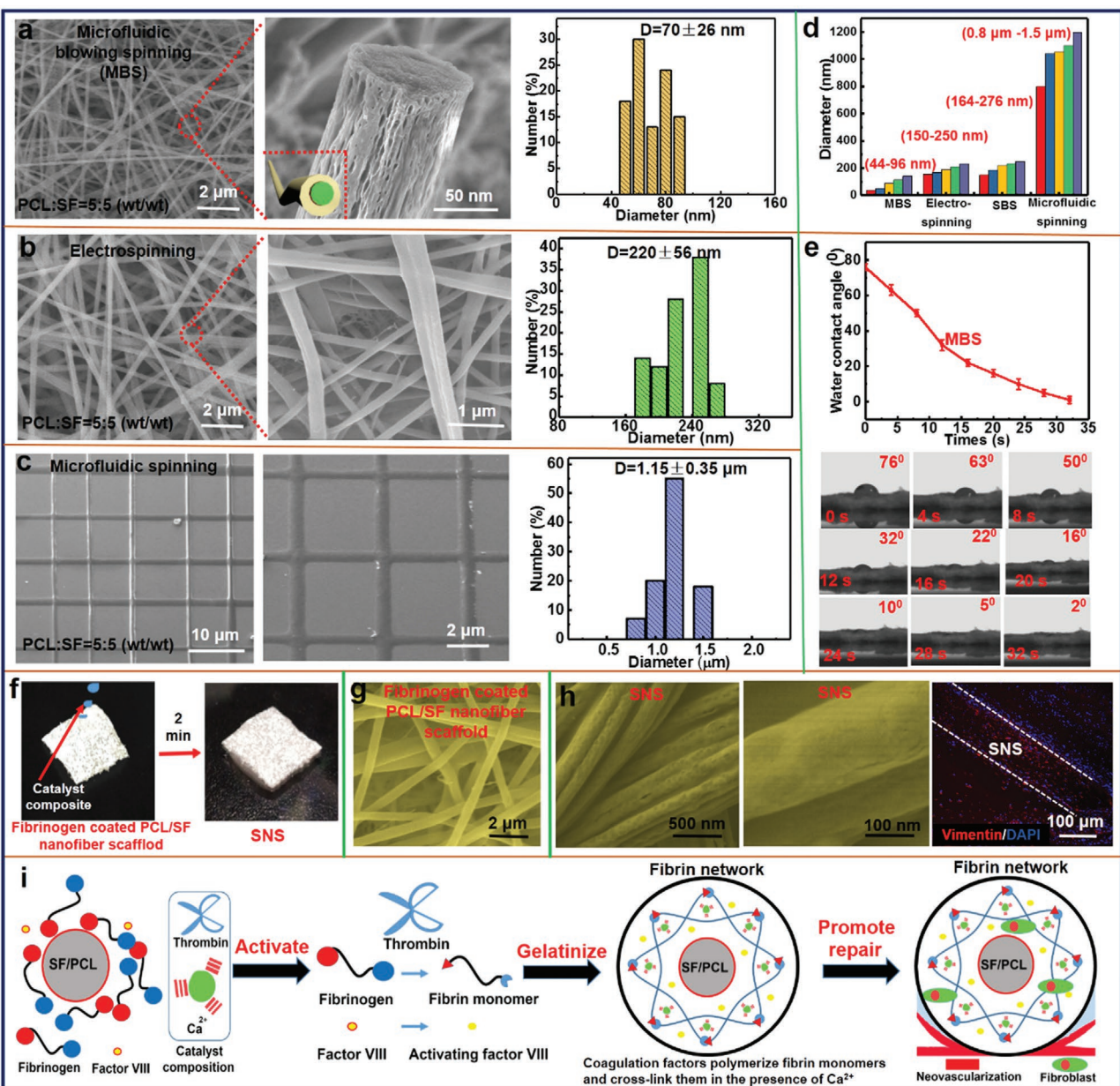


Figure 2. Characterizations of nanofiber scaffolds and formation of SNS. a–c) SEM images and diameter distributions of nanofibers prepared by different spinning techniques: a) MBS, b) electrospinning, and c) microfluidic spinning. d) Comparison of fiber diameter of nanofibers prepared by four spinning methods (electrospinning, SBS, microfluidic spinning, MBS). e) Curves (upper) and images (lower) for temporal evolution of water contact angle of fibrinogen-coated nanofiber scaffolds. f) Digital photographs of fibrinogen-coated PCL/SF nanofiber scaffolds (left) and SNS (right). g) SEM images of nanofiber scaffolds. h) SEM images of SNS in which nanofibers were bonded together in a cluster (left, middle) and the fluorescence double staining image of SNS (right). i) Mechanism of the reaction between the thrombin and the fibrinogen on the surface of PCL/SF nanofiber to form a SNS and the migration of fibroblasts.

to form fibrin sealant, and then it finally forms SNS. Among them, fibrinogen is cleaved by thrombin to yield fibrin, which then coagulates to form fibrin networks (Figure 2i). Figure S17, Supporting Information, shows the FT-IR spectra of the fibrinogen-coated nanofiber scaffold before and after adding the catalyst composite (containing thrombin). We can see that there are mainly $-\text{COOH}$ (1737 cm^{-1}) and $-\text{NH}_2$ (3455 cm^{-1}) groups in fibrinogen-coated PCL/SF nanofiber scaffold, but peptide bond ($\text{CO}-\text{NH}-$, 1641 cm^{-1}) appears after adding catalyst

composite to form SNS. This indicates the successful reaction between fibrinogen and thrombin, which is consist with the reported literature.^[45] Consequently, as compared to traditional nanofiber scaffolds^[4] and hydrogels,^[7] the as-prepared SNS not only exhibits advantages of excellent mechanical strength and good degradability, but also have high specific surface area, high porosity, good gas permeability and superior wettability.

The next set of experiments focused on the biocompatibility, hemostatic and promoting angiogenesis function of SNS.

The results present that the cell viability of SNS could remain 90% after 3 days (Figure S18, Supporting Information), indicating the SNS shows good cytocompatibility and nontoxicity by cell culture of L929 fibroblasts on SNS. This is due to the biocompatibility of PCL, SF and fibrin sealants, and the degradation products are not toxic to main organs of animals.^[13,16,37] We then transplanted SNS to the subcutaneous part of the rat back. The SNS can be directly attached to the wounds based on the strong adhesion of the outer fibrin sealant. The skin of the rat back was cut at different times to investigate the repair process of rat back vascular hemorrhage *in vivo* (Figure 3a). The local hemorrhage was quickly stopped with the treatment of SNS, which can directly provide a platelet aggregation scaffold, thus accelerating local hemostasis (Figure 3b). In addition, considering the fibrin sealant can promote the proliferation and migration of vascular endothelial cells,^[46] we compared the effect of PCL, SF, fibrin sealant and SNS on the proliferation of vascular endothelial cells, respectively (Figure S19, Supporting Information). We found that fibrin sealant can promote the proliferation of vascular endothelial cells, but the efficiency is not high. However, SNS can greatly improve the proliferation ability of vascular endothelial cells because the ultrafine nanofiber gives fibrin sealant a high specific surface area. Moreover, new blood vessels began to form on day 5 and a complete vascular network generated on day 7, further indicating that the SNS exhibits good biocompatibility, the formed fibrin sealant has a certain ability to promote angiogenesis (Figure 3c). The formation principle of fibrin sealant is derived from the coagulation process (fibrinogen–fibrin monomer–fibrin polymer–interaction network). Fibrin sealant can directly form clots with blood cells and platelets at the damaged blood vessels,^[47] shortening the clotting time and achieving rapid hemostasis. The fibers on SNS surface are wrapped of fibrin sealant, which will cover a fibrin sealant mesh outside the damaged blood vessel, directly forming a clot for rapid hemostasis. To further confirm the excellent hemostasis property, a rat model of liver injury with a cross-cut was performed to simulate severe trauma. It was found that the wound was bleeding freely with a large area of blood accumulating on the wiping paper within 15 s (Figure 3d). Interestingly, when the SNS was attached on the wound as a physical barrier, blood loss was almost stopped within 15 s (Figure 3d; Movie S2, Supporting Information). These results further confirm that the SNS demonstrates excellent hemostatic effect, which is of great significance for wound healing, especially for acute massive bleeding.

Another investigation focused on the fibroblast proliferation and migration-induced SNS skin tissue formation. The hematoxylin and eosin (H&E) staining shows large number of cells coverage on the SNS surface after 1 day in culture, and normal connective tissues formed on day 7 (Figure 3e). Masson's trichrome fluorescence staining shows that the amount of collagen around SNS increased significantly from day 5 to day 7 (Figure 3f). Additionally, the results of cell experiments show that fibrin sealant in core–shell structure nanofiber scaffold could significantly increase the expression of F-actin in fibroblasts compared with other forms (PCL/SF, fibrin sealant (FS) and fibrin sealant at PCL/SF nanofiber scaffold (FS@PCL/SF)) (Figure S20, Supporting Information), indicating that SNS could increase the movement ability of fibroblasts and accelerate their migration. Therefore, these results reflect the preferential

properties of dermal-imitating SNS-based nanofibers (fiber diameter, pore diameter, and stiffness are shown in Figure 2 and Figure S9, Supporting Information). Furthermore, we used α -smooth (green) to label blood vessels. It is worth noting that the neovascularization begins on day 3 and forms a complete tubular vessel on day 5 (Figure 3g). These results suggest that the SNS promotes angiogenesis, fibroblast proliferation and migration, which could be attributed to the role of fibrin sealant,^[43,46] leading to the reconstruction of skin tissue.

We then systematically studied the neovascularization and the tissue structure to further confirm the new generation of skin tissue by aid of H&E staining and immunofluorescence staining. Initially, we designed four sets of experiments, namely PCL/SF scaffold group (composition is fibrinogen, PCL, SF), fibrin sealant group (composition is fibrinogen, thrombin), FS@PCL/SF (fibrin sealant adheres to PCL/SF nanofiber scaffold) and SNS (thrombin and fibrinogen undergo gelation reaction on PCL/SF nanofibers to form SNS) group, which were implanted subcutaneously in the back of the rat, respectively. The specimens were taken on the 1st, 5th, and 15th days for investigation of the skin tissue. For the PCL/SF scaffold group (Figure 4a), a large number of cells accumulated around the scaffold (Figure 4a-1), which were determined to be inflammatory cells by immunofluorescence staining (Figure 4a-2). This feature indicates a significant stimulation on the wound, which may lead to excessive body immunity. Whereas, a very small amount of inflammatory cells aggregation was found in the fibrin sealant (FS) group, FS@PCL/SF group and the SNS group (Figure 4b-2,c-2,d-2), indicating little irritation of FS to the wounds. This may be due to the good biocompatibility of fibrin sealant, which does not cause the aggregation of inflammatory cells. Moreover, we found that the organizational structure of the four groups had some changes (Figure 4a–d-3). Therefore, we utilized the fluorescent staining to observe the formation and distribution of blood vessels (Figure 4a–d-4). For PCL/SF group, it couldn't promote the regeneration of the blood vessels in the opposite side of the membrane (Figure 4a-4); the fibrin sealant group achieved uniform vascular distribution (Figure 4b-4); FS@PCL/SF had similar results as PCL/SF (Figure 4c-4); for the SNS group, blood vessels were formed on both sides of the SNS (Figure 4d-4). In addition, we also analyzed the tissue structure of the four groups (Figure 4a–d-5). For the PCL/SF group, the wound was significantly stimulated, resulting in excessive tissue growth around the nanofiber scaffold (Figure 4a-5), and the fibrin sealant was difficult to distinguish from the surrounding tissue (Figure 4b-5). With the loss of the fibrin sealant in the FS@PCL/SF group, the exposed fibers also began to stimulate the tissue, which resulted in a slight tissue hyperplasia (Figure 4c-5). And interestingly, the tissue surrounding the SNS was clearly aligned (Figure 4d-5). Besides, we further observed the collagen distribution of the new tissue in each group by fluorescent staining (Figure 4a–d-6). In these four groups, we found that only SNS collagen was arranged regularly and distributed more evenly (Figure 4d-6). We speculate that this is due to the direct action of PCL/SF nanofibers on tissues, resulting in a lack of tissue protection, but fibrin sealants have been an excellent tissue engineering material without stimulating the tissue. Second, the raw materials of the FS@PCL/SF and SNS groups are the same, but due to the different combination of sealant and fiber (the fibrin sealant is directly

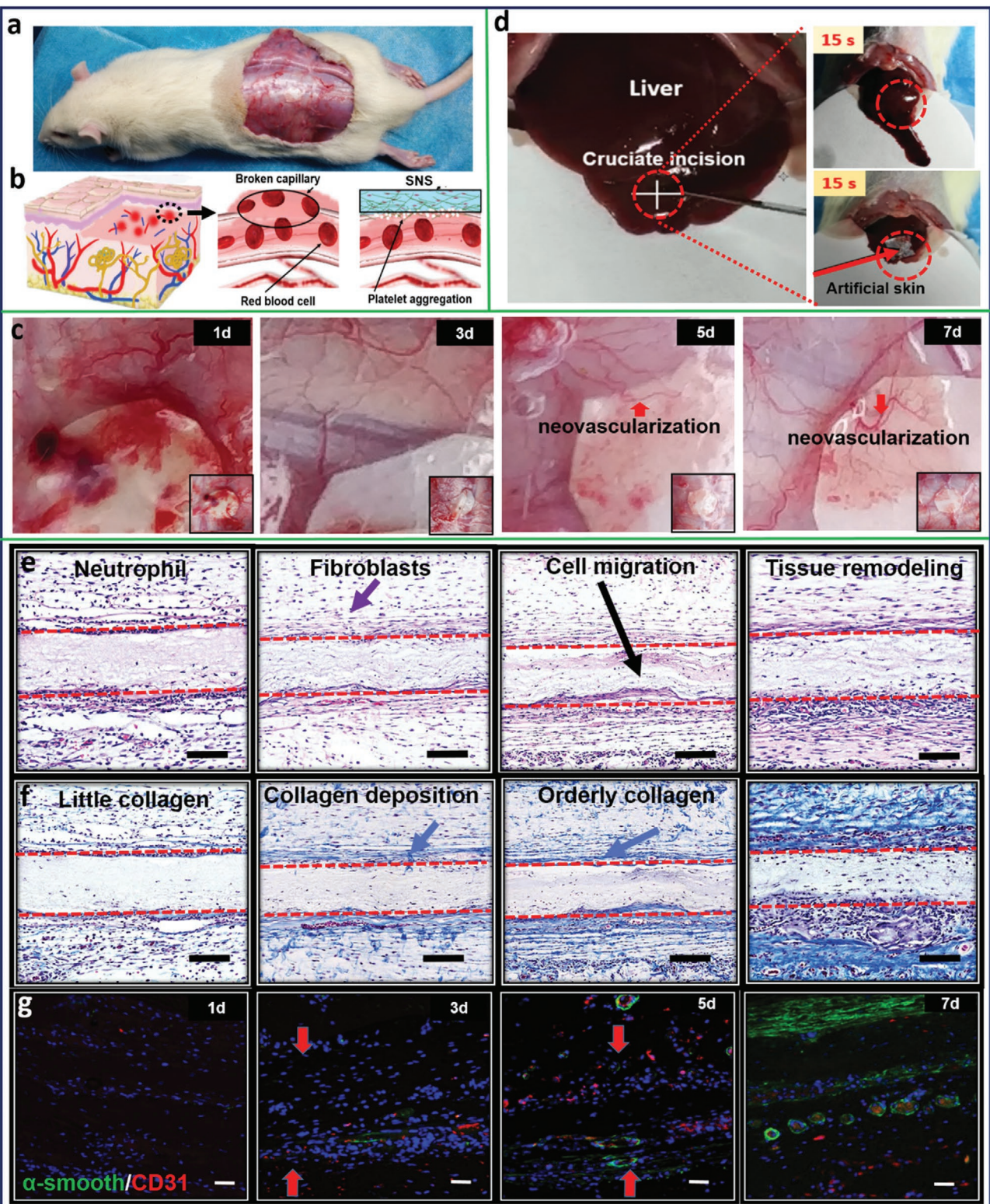


Figure 3. In vivo study of the process (fibroblast proliferation and migration, normal connective tissue formation, collagen deposition, and neovascularization) of skin tissue reconstruction. a) Photograph of a mouse with a large area wound on the back. b) Schematic illustration for hemostasis of small vessels bleeding on wound surface treated with SNS. c) Overviews of SNS encapsulated in tissue after its implantation into the damage area on the rat back for 1, 3, 5, and 7 days. (The red arrow indicate blood vessels). d) Bleeding model images of rat liver: a cross-cut in the liver of the rat (left), rat liver injury bleeding (top right) and hemostasis by SNS (right down). e) H&E staining, f) Masson staining, and g) fluorescent staining of SNS-implanted area on days 1, 3, 5, and 7. The red line indicates the SNS area, and purple, black, and blue arrows indicate fibroblasts, fibroblasts migrate to the SNS area and collagen deposition, respectively. Scale bar: 100 µm.

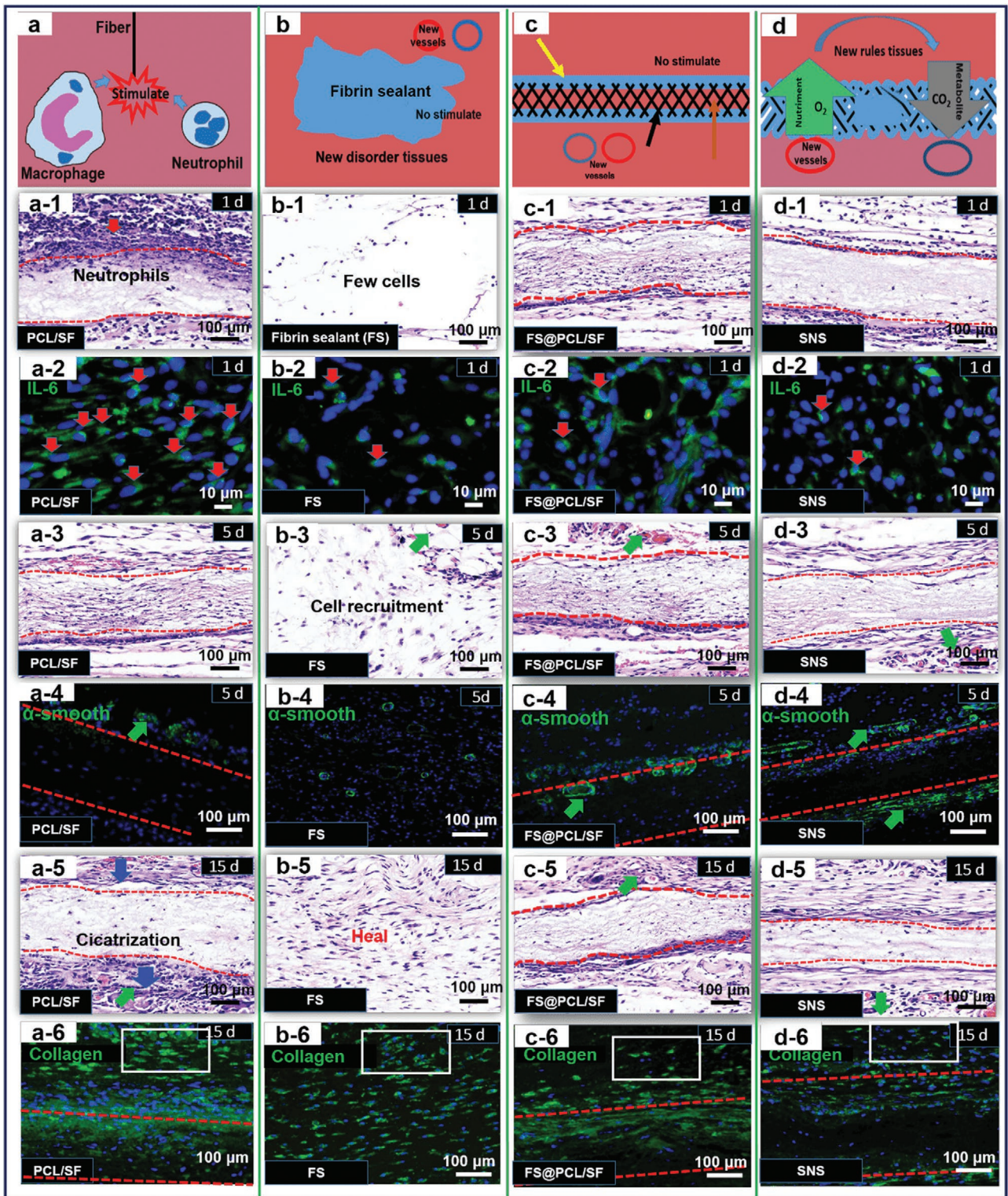


Figure 4. H&E staining (1, 3, 5), inflammatory cell fluorescent staining (2), vessels fluorescent staining (4), and collagen fluorescent staining (6) of the tissues around the implantation sites during different periods. a) PCL/SF nanofiber scaffold system. Red arrow points to inflammatory cells and blue arrow points to scar tissue. b) Fibrin sealant system. No immune response and disordered structure were observed. c) FS&PCL/SF system, green arrow points to the neovascularization. d) Fibrin sealant loaded nanofiber scaffold (SNS) system. Red lines mark the boundaries of tissues and materials. The area in the white box represents normal tissue (yellow arrows, orange arrows, and black arrows in the schematic diagram represent the fibrin sealant, tissue, and fibrinogen-coated PCL/SF nanofibers, respectively).

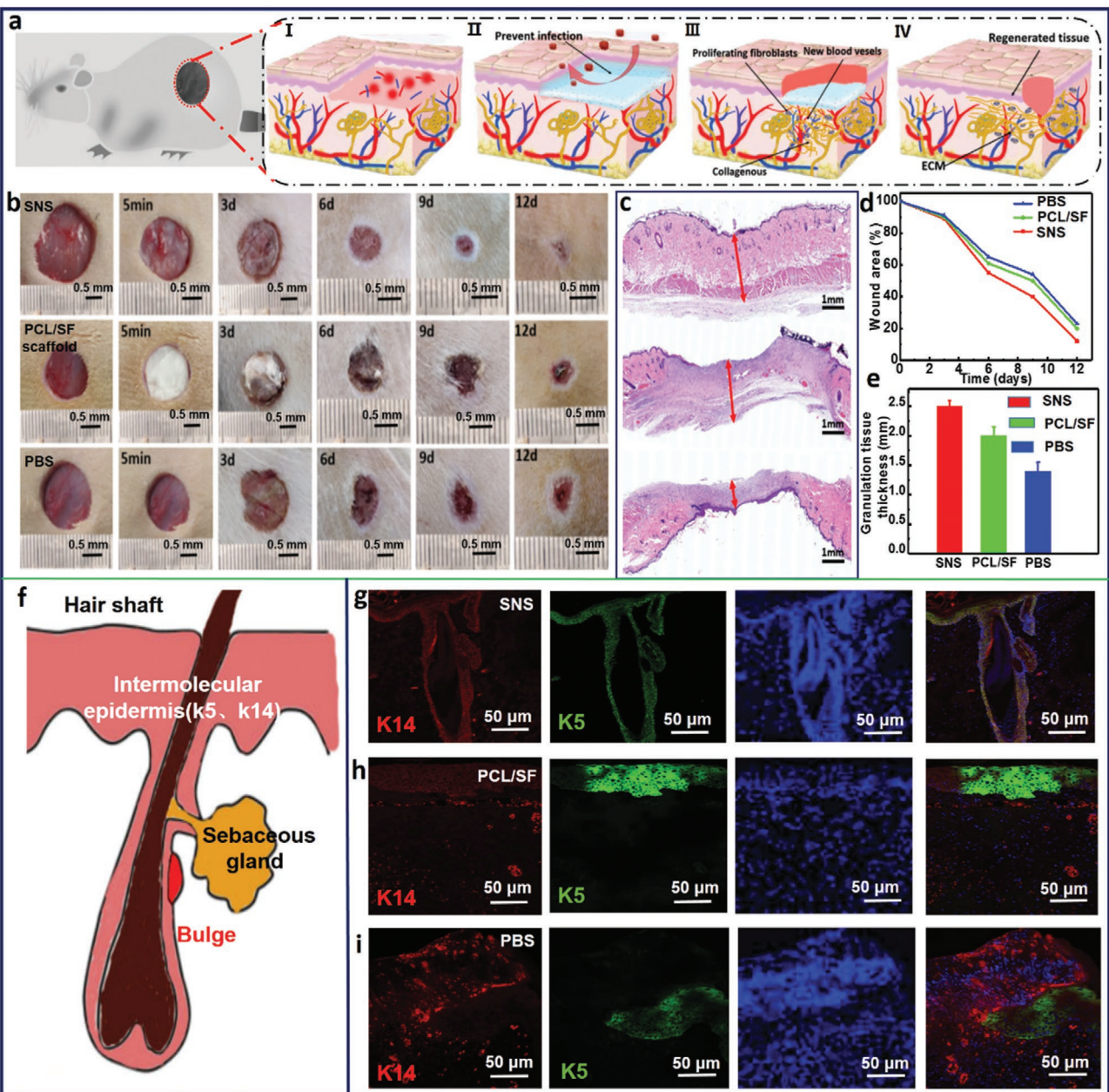


Figure 5. Three processes (wound healing area, granulation growth thickness, and hair follicle formation) of skin formation. a) Schematic illustrations of wound healing process. b) Digital photographs of representative skin wound healing processes in rats treated with SNS, PCL/SF nanofiber scaffold, and PBS, respectively. c) Microscopy images of granulation growth of SNS, PCL/SF nanofiber scaffold, and PBS groups stained by H&E. d) Plots of wound area size versus time. e) Quantitative analysis of granulation tissue thickness. f) A simple sketch of hair follicle structure. g-i) Double immunofluorescence staining of K14 and K5 of the neonatal tissue for SNS (g), PCL/SF nanofiber scaffold (h), and PBS (i), respectively.

applied to the fiber membrane in the FS@PCL/SF group, and the fibrin sealant is formed *in situ* on the nanofibers in the SNS group, the specific surface area of the sealant of FS@PCL/SF is much lower than SNS. Therefore, the effect of SNS is significantly better than the other three groups. As evidenced by neovascularization and the formation of orderly tissue structure, the transmutation of SNS into skin tissue is successfully accomplished. These findings imply that the SNS shows distinct advantages in formation of tissue, which further promotes the skin tissue reconstruction.

To assess the formation of the skin regeneration, systematic analysis was carried out by quantifying the size of wound healing area, the growth thickness of granulation along with the formation of hair follicles (Figure 5a). We designed three sets of experiments (SNS group, PCL/SF scaffold group and the phosphate buffered saline (PBS) group) for investigation of wound healing process. As shown in Figure 5b,d, the wound treated with SNS was almost healed after 12 days (healing efficiency of 90%), while the healing efficiency of those treated with PCL/SF scaffold (healing efficiency of 80%) and PBS (healing efficiency

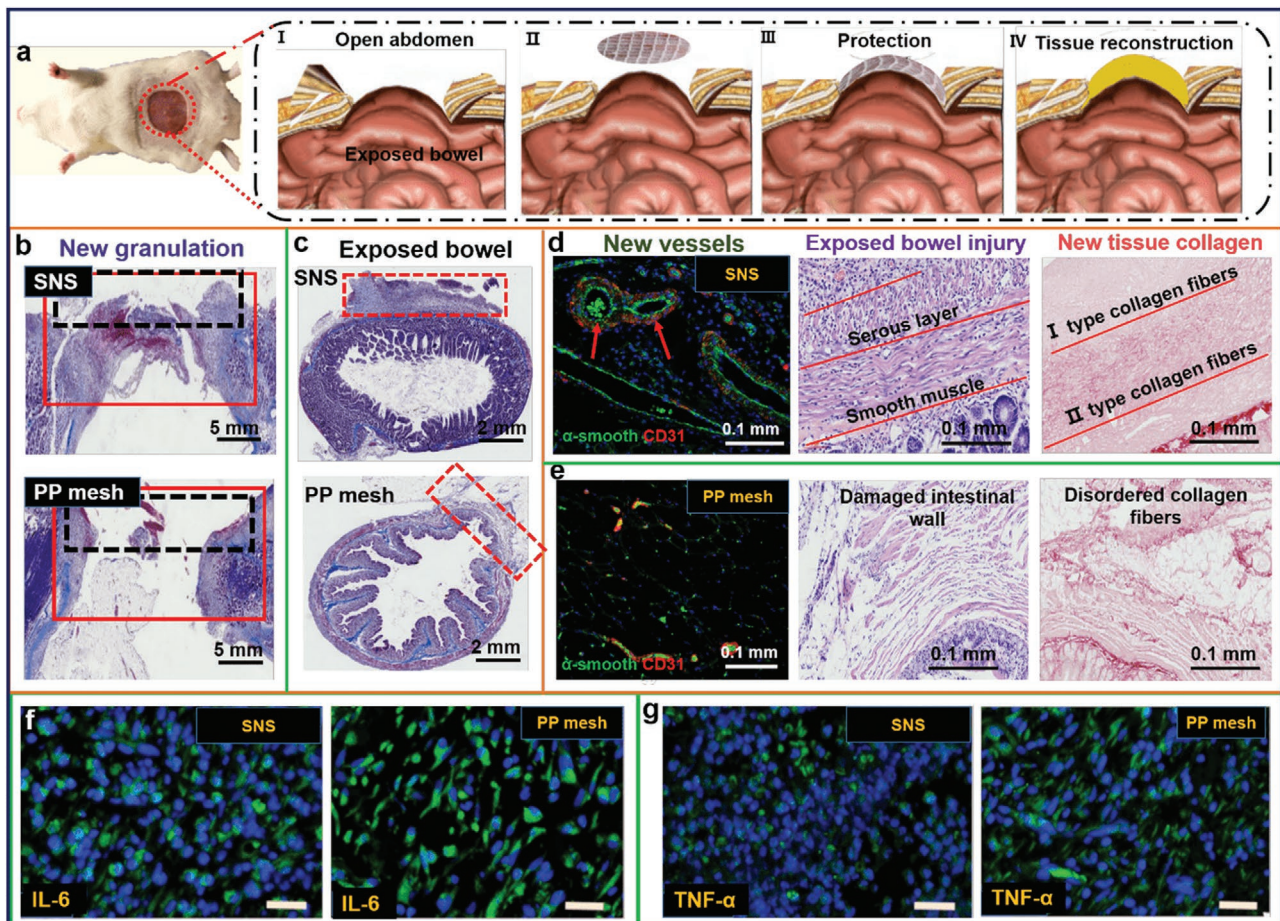


Figure 6. Application of SNS. a) Schematic illustration of early protection and tissue regeneration. b) Mason staining of the neonatal tissues and the exposed intestinal canal in both groups of SNS and PP mesh (the red border indicates the injured area and the black border indicates the SNS- or PP mesh-covering area). c) The exposed intestinal canal in the SNS group (top) and PP mesh group (down) (the red border indicates the SNS- or PP mesh-covering area). d,e) H&E staining and Sirius red staining of abdominal wall defect treated with SNS (d) and PP mesh (e): new blood vessels (red arrow markers) (left); new tissue structure in neonatal tissues (middle) and collagen fibers (right). f,g) Immunofluorescence staining of IL-6 (f) and TNF- α (g) in regenerative tissues on abdominal wall defect implanted with artificial skin and PP mesh, respectively. Scale bar: 100 μ m.

of 77%) was obviously much lower with blood clot scab. The results revealed that the SNS could accelerate cutaneous wound healing. In addition, we conducted histological analysis of the healed skin tissue. From the perspective of granulation growth of wounds, it was found that the granulation growth thickness of the SNS group (2.4 mm) was significantly higher than those of the other two groups (2 mm for PCL/SF group; 1.3 mm for PBS group), as shown Figure 5c,e. In addition, through the double immunofluorescence staining experiments (Figure S21, Supporting Information), we observed a relatively complete structure along with the emergence of new hair follicles for SNS group. While a large amount of collagen deposition suggests the formation of scar tissue for PCL/SF nanofiber scaffold group. These results indicate that the SNS offers great potential in accelerating wound healing, as well as provides huge significance in clinical applications. Moreover, we thoroughly investigated the hair-follicle-like structure in the neonatal tissue to further verify the formation of skin, where K14 and K5 were utilized to label the hair follicle structure (Figure 5f). We noted that the hair follicle structure of the neonatal tissue for SNS group

was complete (Figure 5g). Whereas, the new tissues for PCL/SF scaffold group formed epidermis without hair follicle structure (Figure 5h). For PBS group, the new tissue structure was hazy (Figure 5i). We speculate that the formation of hair follicles is due to the improvement of blood supply (promoting angiogenesis) and cell migration of new granulation tissue by SNS.^[48,49] Moreover, SNS can fully cover the wound, protect the new granulation at the wound, and reduce the influence of external uncontrolled environment on wound healing. The above results suggest the successful formation of skin regeneration by SNS.

Abdominal skin defect refers to the abdominal wall defect, which leads to the exposure of abdominal organs,^[50] easy infection, no nutrients and scaffold supporting. In turn, these issues will hamper the healing and regeneration of abdominal skin. Therefore, protecting the exposed intestine has been a big challenge for surgeons in the world.^[51] Here, we employed the as-fabricated SNS for large area abdominal skin defect in rats, along with the investigation of its important role in early protection, anti-infection, wound healing and skin regeneration (Figure 6a). We divided the experiments into two groups, one for

the SNS group and the other for the polypropylene (PP) mesh group. Typically, the operation of abdominal cavity contains four stages, namely opening abdominal skin, opening abdominal wall, covering the defect and forming collagen protection (Figure S22, Supporting Information). Interestingly, for SNS group, a new tissue on the intestinal wall along with collagen protective layer generated after 7 days without destroying its original intestinal wall structure while no similar tissue reconstruction was observed in the case of PP mesh (Figure 6b,c). For further investigation of the new tissues, we systematically analyzed the H&E staining, Masson trichrome staining, and Sirius red staining. It is obvious that a large amount of microvascular could be observed in the dermis of the SNS group (red arrow markers, Figure 6d, left), while there are no microvascular observed in the control group. Additionally, the SNS group also shows smooth surfaces (Figure 6d, middle) and abundant uniform collagen arrangement with type I collagen along with type II collagen (Figure 6d right), which are almost identical to the normal skin. This phenomenon may be attributed to the regulation of fibroblast arrangement, leading to the regular pattern arrangement of collagen. Whereas, in terms of PP mesh group, edema, ruptured smooth muscle, destroyed serosa layer and disordered collagen fibers were observed, indicating that the intestinal wall may be damaged (Figure 6e). All the above results demonstrate that the as-fabricated SNS acts an important role in early protection, wound healing, and skin regeneration.

In addition, wound infection is a serious threat to wound healing, and the lack of wound protection is one of the main causes of infection.^[52] The best solution to this problem is to avoid infection, and the SNS can effectively protect the wound to prevent the wound from being invaded by external infection sources. In this case, we selected two typical pro-inflammatory factors, interleukin-6 (IL-6) and tumor necrosis factor (TNF- α), and studied the ability to reduce the incidence of wound infections of SNS by immunohistochemistry. One week after treatment, we tested IL-6 and TNF- α in the control group (PP mesh) and the experimental group (SNS group), respectively, as shown in Figure 6f,g. There were a large amount of IL-6 and TNF- α in the control group, which indicates that severe inflammatory reactions occurred. In contrast, much less IL-6 and TNF- α were detected in the SNS group, displaying a slight inflammatory response (Figure S23, Supporting Information). Consequently, the SNS shows great advantages and clinical significance in terms of large area wound healing, wound protection, and tissue regeneration (reepithelialization, epidermal thinning, collagen alignment) due to its inherent biocompatibility, degradability, high mechanical strength, and high biomimetic structural characteristics.

In summary, we propose a versatile strategy for formation of large-area robust skins by a three-stage transformation process: fabrication of a biodegradable fibrin-sealant-loaded nanofiber scaffold (SNS), skin tissue construction, and skin regeneration formation. Initially, the fabrication of nanofiber scaffolds is conducted via MBS technique. The MBS method shares several key advantages: allowing the fabrication of ultrafine fibrinogen-coated PCL/SF core–shell nanofiber with an average diameter of 65 nm; providing a facile way toward a large-area nanofiber scaffold ($140 \times 40 \text{ cm}^2$) with large specific surface

area, excellent gas permeability, and strong tensile strength, which offer great potential for further use as skin regeneration. The as-prepared SNS possesses superior mechanical strength, wettability, and excellent cell adhesion, promoting the recruitment and proliferation of fibroblasts to form a skin tissue. In vivo experiments indicate that it promotes collagen deposition, neovascularization, as well as granulation tissue, hair follicles, and new regular tissue construction to easily form skin. More importantly, we apply the large-area SNS to the abdominal skin defect; the results demonstrate that the SNS has excellent protective and anti-infection abilities and promotes the tissue regeneration. In general, we demonstrate a proof-of-concept of a new kind of skin regeneration derived from SNS. This robust skin regeneration could be achieved by the migration of fibroblasts on the fibrin sealant loaded PCL/SF nanofiber scaffold. This can not only effectively solve the medical problem of large-area abdominal trauma, but also avoid the risk of immune rejection and secondary surgery in clinical applications.

Supporting Information

Supporting Information is available from the Wiley Online Library or from the author.

Acknowledgements

T.T.C. and J.F.Y. contributed equally to this work. This work was supported by National Natural Science Foundation of China (21736006, 81870396, 21978132, 21908103), Natural Science Foundation of Jiangsu Province (BK20190672), Fund of State Key Laboratory of Materials-Oriented Chemical Engineering (ZK201704, ZK201716), Priority Academic Program Development of Jiangsu Higher Education Institutions (PAPD), and the Social Development Projects for Key Research and Development Plan in Jiangsu Province (BE2017725). This study was carried out according to the Recommendations of Guidelines for Clinical Trials by the Ethics Committee of Jinling Hospital. All animal experiments in our study were performed according to the principles of the Declaration of Helsinki, and were approved by the Animal Ethical Committee of Jinling Hospital (2018GKJDWLS-03-127).

Conflict of Interest

The authors declare no conflict of interest.

Keywords

abdominal wall defects, microfluidic-blown-spinning, skin regeneration

Received: February 11, 2020

Revised: May 28, 2020

Published online: July 6, 2020

- [1] D. J. Tobin, *Chem. Soc. Rev.* **2006**, *35*, 52.
- [2] Q. X. Ye, P. Tao, C. Chang, L. Y. Zhou, X. L. Zeng, C. Y. Song, W. Shang, J. B. Wu, T. Deng, *ACS Appl. Mater. Interfaces* **2019**, *11*, 3417.
- [3] Q. Wang, M. Q. Jian, C. Y. Wang, Y. Y. Zhang, *Adv. Funct. Mater.* **2017**, *27*, 1605657.

- [4] S. Ahn, C. O. Chantre, A. R. Gannon, J. U. Lind, P. H. Campbell, T. Grevesse, B. B. O'Connor, K. K. Parker, *Adv. Healthcare Mater.* **2018**, *7*, 1701175.
- [5] S. Kandhasamy, S. Perumal, B. Madhan, N. Umamaheswari, J. A. Banday, P. T. Perumal, V. P. Santhanakrishnan, *ACS Appl. Mater. Interfaces* **2017**, *9*, 8556.
- [6] J. Qu, X. Zhao, Y. P. Liang, T. L. Zhang, P. X. Ma, B. L. Guo, *Biomaterials* **2018**, *183*, 185.
- [7] M. A. Darabi, A. Khosrozadeh, R. Mbeleck, Y. Q. Liu, Q. Chang, J. Z. Jiang, J. Cai, Q. Wang, G. X. Luo, M. Xing, *Adv. Mater.* **2017**, *29*, 1700533.
- [8] S. Kim, S.-G. Park, S.-W. Kang, K. J. Lee, *Macromol. Mater. Eng.* **2016**, *301*, 818.
- [9] H.-E. Thu, M. H. Zulfakar, S. F. Ng, *Int. J. Pharm.* **2012**, *434*, 375.
- [10] Y.-M. Kook, H. Kim, S. Kim, K. Lee, C. Y. Heo, M. H. Park, W.-G. Koh, *Nanomaterials* **2018**, *8*, 117.
- [11] M. Kurita, T. Araoka, T. Hishida, D. D. O'Keefe, Y. Takahashi, A. Sakamoto, M. Sakurai, K. Suzuki, J. Wu, M. Yamamoto, R. Hernandez-Benitez, A. Ocampo, P. Reddy, M. N. Shokhirev, P. Magistretti, E. N. Delicado, H. Eto, K. Harii, J. C. I. Belmonte, *Nature* **2018**, *561*, 243.
- [12] J. Ding, J. Zhang, J. Li, D. Li, C. Xiao, H. Xiao, H. Yang, X. Zhuang, X. Chen, *Prog. Polym. Sci.* **2019**, *90*, 1.
- [13] C.-H. Chen, S.-H. Chen, C.-Y. Kuo, M.-L. Li, J.-P. Chen, *Nanomaterials* **2017**, *7*, 219.
- [14] T. Xu, H. Y. Yang, D. Z. Yang, Z. Z. Yu, *ACS Appl. Mater. Interfaces* **2017**, *9*, 21094.
- [15] M. Zhang, X. Q. Li, S. Li, Y. J. Liu, L. L. Hao, *J. Mater. Sci.: Mater. Med.* **2016**, *27*, 136.
- [16] C. Steffi, D. Wang, C. H. Kong, Z. Y. Wang, P. N. Lim, Z. L. Shi, E. S. Thian, W. Wang, *ACS Appl. Mater. Interfaces* **2018**, *10*, 9988.
- [17] A. R. Sadeghi, S. Nokhasteh, A. M. Molavi, M. Khorsand-Ghayeni, H. Naderi-Meshkin, A. Mahdizadeh, *Mater. Sci. Eng., C* **2016**, *66*, 130.
- [18] B. N. Blackstone, J. W. Drexler, H. M. Powell, *Tissue Eng., Part A* **2014**, *20*, 2746.
- [19] J.-P. Chen, G.-Y. Chang, J.-K. Chen, *Colloids Surf. A* **2008**, *313*-314, 183.
- [20] B. K. Sun, Z. S. Siprashvili, P. A. Khavaril, *Science* **2014**, *346*, 941.
- [21] Z. P. Rad, J. Mokhtari, M. Abbasi, *Mater. Sci. Eng., C* **2018**, *93*, 356.
- [22] M. V. Plikus, C. F. Guerrero-Juarez, M. Ito, Y. R. Li, P. H. Dedhia, Y. Zheng, M. Shao, D. L. Gay, R. Ramos, T.-C. Hsi, J. W. Oh, X. J. Wang, A. Ramirez, S. E. Konopelski, A. Elzein, A. Wang, R. J. Supapannachart, H.-L. Lee, C. H. Lim, A. Nace, A. Guo, E. Treffiesen, T. Andl, R. N. Ramirez, R. Murad, S. Offermanns, D. Metzger, P. Chambon, A. Hamilton, S. E. Millar, P. Seale, W. S. Pear, M. A. Lazar, G. Cotsarelis, *Science* **2017**, *355*, 748.
- [23] N. Hibino, C. A. Best, A. Engle, S. Ghimbovschi, S. Knoblauch, D. S. Nath, N. Ishibashi, R. A. Jonas, *Tissue Eng., Part A* **2016**, *22*, 75.
- [24] G. Ajmal, G. V. Bonde, P. Mittal, G. Khan, V. K. Pandey, B. V. Bakade, B. Mishra, *Int. J. Pharm.* **2019**, *567*, 118480.
- [25] D. W. Song, S. H. Kim, H. H. Kim, K. H. Lee, C. S. Ki, Y. H. Park, *Acta Biomater.* **2016**, *39*, 146.
- [26] W. K. Hu, Z. J. Wang, Y. Xu, X. H. Wang, Y. Xiao, S. M. Zhang, J. L. Wang, *J. Mater. Chem. B* **2019**, *7*, 3412.
- [27] C. H. Zhu, J. H. Zhu, C. W. Wang, R. Chen, L. Sun, C. H. Ru, *IEEE Trans. Nanotechnol.* **2018**, *17*, 675.
- [28] J. Xue, T. Wu, Y. Dai, Y. Xia, *Chem. Rev.* **2019**, *119*, 5298.
- [29] X. Yang, J. Yang, L. Wang, B. Ran, Y. Jia, L. Zhang, G. Yang, H. Shao, X. Jiang, *ACS Nano* **2017**, *11*, 5737.
- [30] H. W. Ju, O. J. Lee, J. M. Lee, B. M. Moon, H. J. Park, Y. R. Park, M. C. Lee, S. H. Kim, J. R. Chao, C. S. Ki, C. H. Park, *Int. J. Biol. Macromol.* **2016**, *85*, 29.
- [31] M. Vural, A. M. Behrens, W. Hwang, J. J. Ayoub, D. Cresce, A. V. W. Cresce, O. B. Ayyub, R. M. Briber, P. Kofinas, *ACS Appl. Mater. Interfaces* **2018**, *10*, 13953.
- [32] Y. R. Yu, F. F. Fu, L. R. Shang, Y. Cheng, Z. Z. Gu, Y. J. Zhao, *Adv. Mater.* **2017**, *29*, 1605765.
- [33] H. Y. Cheng, J. K. Meng, G. Wu, S. Chen, *Angew. Chem., Int. Ed.* **2019**, *58*, 17465.
- [34] Y. Zhang, C.-F. Wang, L. Chen, S. Chen, A. J. Ryan, *Adv. Funct. Mater.* **2015**, *25*, 7253.
- [35] E. Hofmann, M. Dulle, X. Liao, A. Greiner, S. Förster, *Macromol. Chem. Phys.* **2019**, *221*, 1900453.
- [36] D. D. da Silva Parize, M. M. Foschini, J. E. de Oliveira, A. P. Klamczynski, G. M. Glenn, J. M. Marconcini, L. H. C. Mattoso, *J. Mater. Sci.* **2016**, *51*, 4627.
- [37] W. D. Spotnitz, S. Burks, *Transfusion* **2012**, *52*, 2243.
- [38] W. Furst, A. Banerjee, *Ann. Thoracic Surge.* **2005**, *79*, 1522.
- [39] B. Mizrahi, C. F. Stefanescu, C. Yang, M. W. Lawlor, D. Ko, R. Langer, D. S. Kohane, *Acta Biomater.* **2011**, *7*, 3150.
- [40] D. G. Wallace, G. M. Cruise, W. M. Rhee, J. A. Schroeder, J. J. Prior, J. Ju, M. Maroney, J. Duronio, M. H. Ngo, T. Estridge, G. C. Coker, *J. Biomed. Mater. Res.* **2001**, *58*, 545.
- [41] A. M. Behrens, N. G. Lee, B. J. Casey, P. Srinivasan, M. J. Sikorski, J. L. Daristotle, A. D. Sandler, P. Kofinas, *Adv. Mater.* **2015**, *27*, 8056.
- [42] B. Khalid, X. P. Bai, H. H. Wei, Y. Huang, H. Wu, Y. Cui, *Nano Lett.* **2017**, *17*, 1140.
- [43] E. Chignier, J. Baguet, B. Dessapt, J. Belleville, Y. Descotes, R. Eloy, *J. Surg. Res.* **1981**, *31*, 415.
- [44] F. Han, Z. X. Zhong, Y. Yang, W. Wei, F. Zhang, W. H. Xing, Y. Q. Fan, *J. Eur. Ceram. Soc.* **2016**, *36*, 3909.
- [45] J. Torbet, J. M. Freyssinet, G. Hudryclergeon, *Nature* **1981**, *289*, 91.
- [46] R. Dardika, B. Shenkman, I. Tamarina, R. Eskaraeva, J. Harsfalvib, D. Varona, A. Inbala, *Thromb. Res.* **2002**, *105*, 317.
- [47] H. H. Versteeg, J. W. Heemskerk, M. Levi, P. H. Reitsma, *Physiol. Rev.* **2013**, *93*, 327.
- [48] K. S. Stenn, L. A. Fernandez, S. J. Tirrell, *J. Invest. Dermatol.* **1988**, *90*, 409.
- [49] M. Cetera, L. Leybova, B. Joyce, D. Devenport, *Nat. Cell Biol.* **2018**, *20*, 541.
- [50] G. L. Carlson, H. Patrick, A. I. Amin, G. McPherson, G. MacLennan, E. Afolabi, G. Mowatt, B. Campbell, *Ann. Surg.* **2013**, *257*, 1154.
- [51] E. R. Fitzpatrick, *Crit. Care Nurse* **2017**, *37*, 22.
- [52] S. Guo, L. A. DiPietro, *J. Dent. Res.* **2010**, *89*, 219.